Process Safety and Environmental Protection 191 (2024) 1239–1253

Contents lists available at ScienceDirect

Process Safety and Environmental Protection

journal homepage: www.journals.elsevier.com/process-safety-and-environmental-protection

Machine learning-aided risk-based inspection strategy for hydrogen technologies

Alessandro Campari [a,*], Chiara Vianello [b], Federico Ustolin [a], Antonio Alvaro [c], Nicola Paltrinieri [a]

[a] Department of Mechanical and Industrial Engineering, Norwegian University of Science and Technology NTNU, Richard Birkelands vei 2b, Trondheim 7034, Norway
[b] Department of Industrial Engineering, University of Padova, Via Gradenigo 6a, Padova 35131, Italy
[c] Department of Materials and Nanotechnology, SINTEF Industry, Richard Birkelands vei 2b, Trondheim 7034, Norway

ARTICLE INFO

Keywords:
Hydrogen pipelines
Component safety
Hydrogen-enhanced fatigue
Machine-learning
Risk-based inspection
Loss prevention

ABSTRACT

Although technically challenging, effective, safe, and economical transport is crucial for enabling a widespread rollout of hydrogen technologies. A promising option to transport large amounts of hydrogen lies in employing retrofitted natural gas pipelines. Nevertheless, H_2-rich environments tend to degrade pipeline steels, reducing their load-bearing capability and accelerating crack propagation. Regular inspection and maintenance activities can preserve the pipelines' integrity and guarantee safe operations. The risk-based inspection (RBI) approach is based on estimating the risk for each component item. It focuses most inspection activities on high-risk components to reduce costs while maximizing the plant's safety and availability. However, the RBI standards do not consider hydrogen-induced degradations and cannot be adopted for industrial equipment operating in H_2 environments. This study proposes a novel ad-hoc methodology for the risk-based inspection planning of hydrogen handling equipment. A machine-learning model to predict the fatigue crack growth in gaseous hydrogen environments is developed and integrated with the conventional RBI approach. The proposed methodology is validated on three pipelines transporting hydrogen and natural gas in different concentrations. The results show how similar operating conditions can determine different degradation rates depending on the environment and highlight how hydrogen-enhanced fatigue can reduce the pipelines' lifetime.

1. Introduction

Mitigating the human impact on the environment and moving towards a sustainable economy require a paradigm change in the energy sector (International Energy Agency, 2023). The global energy transition demands clean and affordable energy sources, and hydrogen has been primarily indicated as a versatile and potentially sustainable energy carrier (Norwegian Ministry of Petroleum and Energy, 2020). It can be produced with near-zero pollutant emissions by water electrolysis and is efficiently used in fuel cell systems or repurposed turbomachines. In addition, hydrogen is one of the few options for long-term clean energy storage, thus supporting the integration of renewable sources in the electricity system (Chatzimarkakis et al., 2021). In this context, an efficient and widespread transport infrastructure is crucial, and using the existing natural gas pipeline network to transport vast amounts of hydrogen seems a promising option (Lipiäinen et al., 2023).

However, adapting the natural gas pipelines for transporting pure hydrogen or hydrogen-natural gas blends presents several technical challenges. One of the most pressing issues is the accelerated material degradation of components exposed to H_2-containing environments. The interaction of most metallic materials (e.g., carbon and low-alloy steels) with compressed gaseous hydrogen can impair their performance and durability. This can lead to early losses of integrity and unintended hazardous releases in the environment (Campari et al., 2023d). The issue of fatigue life reduction is particularly severe for large-scale transport pipelines. These systems often have geometrical imperfections and welding defects that can trigger crack initiation and propagation. Even if pipelines should not be subjected to severe load cycles, the number of fatigue failures in industrial practice contradicts this observation (European Gas Pipeline Incident Data Group, 2018; Pipeline and Hazardous Materials Safety Administration, 2022). The lack of proper pipe supports, chattering pressure relief devices, pressure fluctuation due to line packing, and off-design conditions could introduce cyclic loads, potentially exacerbating the risk of failure of pipeline

* Corresponding author.
E-mail address: alessandro.campari@ntnu.no (A. Campari).

https://doi.org/10.1016/j.psep.2024.09.031
Received 3 June 2024; Received in revised form 9 August 2024; Accepted 7 September 2024
Available online 14 September 2024

systems.

Inspection and maintenance activities are crucial to guarantee pipeline integrity and safe operations. Preventive strategies are preferable for handling and transporting hazardous substances, such as pure hydrogen or hydrogen-natural gas blends. The likelihood of severe accidents can be dramatically reduced by putting ad-hoc inspection activities into action (Abbassi et al., 2022). Inspection planning strategies evolved over the years, moving from time or condition-based (Zou et al., 2019) to risk-based approaches (Li et al., 2024). Risk-based inspection (RBI), developed by the American Petroleum Institute, is the most beneficial decision-making methodology for inspection and maintenance planning (American Petroleum Institute, 2019). RBI operates on the understanding that risk is not uniformly distributed among the plant's components, with a limited number of items accounting for a significant portion of the total risk. Inspection and maintenance activities are strategically deployed to maintain the total risk within acceptable limits. By ranking the probabilities and consequences of failure, RBI prioritizes the inspection of high-risk components, thereby optimizing inspection intervals based on acceptable risk levels. This approach maximizes plant safety and reliability and minimizes maintenance costs, providing a significant financial benefit. If properly implemented, this strategy can reduce the probability of equipment failure and implement measures to mitigate the consequences in the case of hazardous releases (Huang et al., 2023).

Nevertheless, the current RBI standards do not consider most hydrogen-induced material degradations. Therefore, unrealistic assumptions must be made when using these guidelines to plan inspections for hydrogen technologies. For instance, Wang et al. (2012) adopted a semi-quantitative RBI for a continuous catalytic steam-methane reforming plant without providing information about the material damages of the components exposed to hydrogen. Defteraios et al. (2020) proposed a risk-based inspection strategy for a hydrogen production plant, determining the failure probability from the results of non-destructive testing (NDT). Even if this approach evaluates the detrimental effects of hydrogen embrittlement and high-temperature hydrogen attack, it is tailored to a specific plant and cannot be generalized for other facilities. Recently, Giannini et al. (2023) adopted an RBI approach for a hydrogen-fueled fishing vessel and highlighted how the existing standards tend to underestimate the risk of failure of hydrogen technologies.

Adaptations of the conventional RBI were proposed to overcome these limitations and qualitatively evaluate the degrading effects of hydrogen embrittlement and hydrogen-enhanced fatigue (Campari et al., 2023a, 2023b). In addition, data-driven approaches were used to predict the hydrogen-induced degradation of tensile properties of aluminum alloys (Thankachan et al., 2017), austenitic steels (Kim et al., 2022), and carbon steels (Campari et al., 2023c; Subedi et al., 2023), or the fracture toughness reduction in martensitic steels (Phan et al., 2021). Given these premises, this study aims to develop a novel risk-based inspection approach for hydrogen technologies. The conventional RBI is integrated with a data-driven model to account for the hydrogen environment's influence on fatigue degradation. Only another example of the combined application of RBI and machine-learning (ML) can be found in the literature. Rachman and Ratnayake, (2019) used a dataset of RBI assessments for oil and gas applications to develop an ML model capable of performing RBI screening assessments. The combination of machine-learning and risk-based inspection of hydrogen technologies has never been explored, but it represents a promising research area.

The paper is structured as follows. In Section 2, the issue of hydrogen-enhanced fatigue in pipeline steels is presented, and the main influencing factors are discussed. Section 3 outlines the fundamentals of the RBI approach, presents the steps to develop the ML classifier, from the database creation to the model evaluation and optimization, and discusses how to integrate the data-driven predictions with the standardized RBI. In Section 4, the proposed methodology is validated and applied to three pipelines carrying different hydrogen and natural gas concentrations but operating under the same loading conditions. In addition, the main findings are presented in Section 5, where the performances of the ML classifier, the risk-based ranking of the components, and the proposed inspection activities are extensively discussed. Finally, Section 6 summarizes the main findings and suggests the direction for future research in the framework of RBI of hydrogen technologies.

2. Hydrogen-enhanced fatigue

Fatigue degradation accounts for 80–90 % of all component failures due to mechanical causes (Fetters, 1964) and is significantly enhanced in hydrogen environments. This enhancement can drastically reduce the lifetime of components subjected to load cycles (Shishime et al., 2008; Suresh and Ritchie, 1982). Pre-existing damages, geometrical imperfections, and stress concentrators could act as crack initiation sites in pipeline systems (Laureys et al., 2022). The hydrogen-enhanced fatigue crack growth rate (HEFCGR) is a result of the synergistic interaction of many factors, such as the hydrogen pressure, temperature, and purity, the microstructure, chemical composition, and strength of the material, and the frequency and amplitude of the load cycles (Barnoush and Vehoff, 2010). Depending on the component's operating conditions, geometry, and material characteristics, it can be three orders of magnitude higher than the fatigue crack growth rate (FCGR) in inert environments (Alvaro et al., 2019).

Hydrogen-induced degradation depends on the concentration of H atoms within the metal lattice, which is proportional to the hydrogen partial pressure. High operating pressures are typical for H_2 transport and storage equipment (Holbrook et al., 1982). Nevertheless, the detrimental effect of high pressures on FCGR varies with the loading conditions and is more prominent for low-amplitude load cycles (Slifka et al., 2018). In addition, temperature influences the hydrogen concentration within the metal lattice. In hydrogen environments, the highest FCGR can be observed at near-ambient temperatures: between 20 and 40 °C for ferritic steels (Takakuwa et al., 2019; Yamabe et al., 2016) and between −10 and 20 °C for high-strength martensitic steels (Gangloff and Wei, 1974). The hydrogen purity also influences the uptake of H atoms within the metal bulk. Some gaseous impurities, such as O_2, CO, and SO_2, are known to hinder the surface reactions, thus mitigating the hydrogen effect on the FCGR (Komoda et al., 2019; Somerday et al., 2013). On the other hand, higher concentrations of CO_2 and CH_4 cannot prevent hydrogen uptake and do not inhibit the HEFCGR (Nelson, 1976).

Microstructural features, such as grain boundaries, inclusions, and other inhomogeneities, significantly affect the materials' compatibility with hydrogen (Campari et al., 2023e). Martensitic steels are prone to hydrogen-enhanced fatigue due to their high residual stresses (Alvaro et al., 2021), while ferritic steels are susceptible to different extents due to their high hydrogen diffusivity (Park et al., 2008). Manufacturing processes, grain refinement, and thermal and surface treatments influence the fatigue performance of materials. Welds and heat-affected zones are particularly critical due to the elevated residual stresses, pre-existing defects, and uncontrolled microstructures (Drexler et al., 2019; Slifka et al., 2015). The chemical composition also influences the material's susceptibility to hydrogen damage. Low-alloy steels with higher carbon, manganese, chromium, molybdenum, vanadium, nickel, and copper contents are less compatible with hydrogen environments (Lancaster, 1999). In contrast, the correlation between material strength and hydrogen-enhanced fatigue remains unclear. Materials with the similar microstructures and different strengths tend to show comparable HEFCGR (Tau et al., 1996).

The mechanical load significantly influences the fatigue performance in H_2 environments. Like all other forms of environmental degradation, HEFCGR tends to increase at lower frequencies (when H atoms have more time to enter the metal and accumulate at the crack tip) (Yamabe et al., 2016). In addition, the amplitude of the load cycles, expressed in

terms of stress ratio (R) and stress intensity range (ΔK), influences the severity of HEFCGR. The former parameter, i.e., the ratio between minimum and maximum stress intensity factors, has a spurious influence (San Marchi et al., 2010). In contrast, the stress intensity range (i.e., the difference between maximum and minimum stress intensity factors) determines the crack propagation regime. At low ΔK, the crack cannot propagate until the stress intensity threshold ΔK_{th} is reached. Above ΔK_{th}, the HEFCGR sharply increases compared to the FCGR in inert environments (Nanninga et al., 2010). In industrial practice, equipment commonly operates under loading conditions with variable frequencies and amplitudes (Zhao et al., 2016).

3. Methodology

The proposed approach to develop a quantitative RBI methodology for equipment exposed to compressed gaseous hydrogen can be divided into four phases:

1. Adoption of the conventional risk-based inspection strategy;
2. Development of a machine-learning model to predict the severity of the hydrogen-enhanced fatigue;
3. Integration of the conventional RBI with the ML predictions;
4. Validation of the methodology on a representative case study.

First, Section 3.1 provides an overview of the conventional RBI strategy. Second, Section 3.2 shows the steps for developing an ML model to predict the effect of hydrogen gas on the fatigue crack growth rate for several plain carbon and low-alloy steels. Third, Section 3.3 explains how the predictions of the ML model can be integrated with RBI to calculate the probability of failure for hydrogen technologies. The combination of these three steps represents the novel *Risk-based Inspection Strategy for Hydrogen technologies* (HyRIS).

3.1. Risk-based inspection

The risk-based inspection method assumes fewer equipment items are responsible for a large share of the total plant's risk. Therefore, inspecting these high-risk components should be a priority to mitigate the overall risk while guaranteeing the preventive measures' cost-effectiveness and minimizing unnecessary downtimes. The RBI approach, as indicated by the recommended practice API 580, has the following structure (American Petroleum Institute, 2016a):

1. Collection of technical information and historical data about the plant;
2. Calculation of the probabilities of failure;
3. Calculation of the consequences of failure;
4. Calculation of the risks;
5. Determination of a risk-based ranking of the components;
6. Definition of the inspection plan.

The first step requires gathering all the information regarding the operating conditions, technical specifications, and inspection history of the plant. Three existing pipelines are used as a case study. The technical characteristics (i.e., geometry, material, manufacturing technique, etc.) and the operating conditions (i.e., nominal pressure, temperature, amplitude and frequency of pressure fluctuations, and flow rates) are considered, assuming to transport either hydrogen, natural gas, or a blend of hydrogen and natural gas and comparing the results.

As a second step, the probability of failure for each component item is calculated through Eq. 1:

$$P_f(t, I_E) = gff \cdot D_f(t, I_E) \cdot F_{SM} \quad (1)$$

where gff is the generic failure frequency, D_f is the damage factor, which is a function of time t and inspection effectiveness I_E, and F_{SM} is the management system factor. The former coefficient indicates the likelihood of failure of an equipment type and is obtained from historical data. API 581 provides the failure frequencies for four different hole sizes (small, medium, large holes, and rupture). The D_f is an adjustment factor for the gff and accounts for the specific characteristics of each component. It depends on the susceptibility to various damage mechanisms, categorized into internal and external thinning, internal and external stress corrosion cracking, high-temperature hydrogen attack, thermal, mechanical, and corrosion fatigue, and embrittlement. These degradation mechanisms can affect the equipment depending on operating conditions and structural material. In addition, the management system factor is a comprehensive index of the effectiveness of the management in maintaining the assets' integrity and operability.

The third step lies in calculating the consequences of failure for each component and each hole size. Given the high flammability and non-toxicicity of hydrogen gas, the impact areas of flammable releases are evaluated. This evaluation considers the thermal radiation for jet fires or fireballs, the overpressure for vapor cloud explosions, and the hydrogen concentration for flash fires. The consequences of each final event are estimated through integral models and consolidated consequence analysis techniques (Baker et al., 1983; CCPS, 2010; Lee, 2001; TNO, 2005). Theoretical release rates are calculated for each hole size. Each potential final event resulting from instantaneous or continuous releases is identified through an event tree analysis. The consequences are then evaluated and weighted on the event probability. Detection and isolation systems also affect the magnitude of the release. The consequence area of a flammable release is calculated using Eq. 2:

$$CA_{flam} = \frac{\sum_{i=1}^{4} gff_n \cdot CA_{flam,n}}{\sum_{i=1}^{4} gff_n} \quad (2)$$

where gff_n and $CA_{flam,n}$ indicate the generic failure frequency and the consequence area of a flammable release from the n-th hole size.

The risk of failure (R_f) for each pipeline leg can be obtained by combining probabilities and consequences of failure (Kaplan and Garrick, 1981), as per Eq. 3:

$$R_f(t, I_E) = P_f(t, I_E) \cdot C_f \quad (3)$$

The risk of each piece of equipment is calculated at the evaluation date, but future risk (i.e., the risk that is predicted after a specific time) can also be estimated. Then, all components are ranked on a risk basis. Equipment exceeding a predefined risk threshold should be inspected and eventually maintained. The optimal inspection techniques are selected depending on the active damage mechanisms, following the recommended practice API 571 (American Petroleum Institute, 2020).

3.2. Machine-learning model

The development of an ML model capable of predicting the effect of a hydrogen environment on the fatigue crack growth rate in low-alloy steels involves five steps:

1. Data collection and pre-processing;
2. Definition of the target attribute;
3. Selection and training of the classifier;
4. Evaluation of the model;
5. Optimization of the model.

The flow diagram in Fig. 1 shows the process from the database creation to the model evaluation. Each step is explained in detail below.

3.2.1. Data collection and cleaning

The results of FCGR tests conducted in hydrogen gas and inert environments are gathered from the literature. The *Technical Database for Hydrogen Compatibility of Materials* (Sandia National Laboratories, 2023) represents the primary source of information. This publicly available

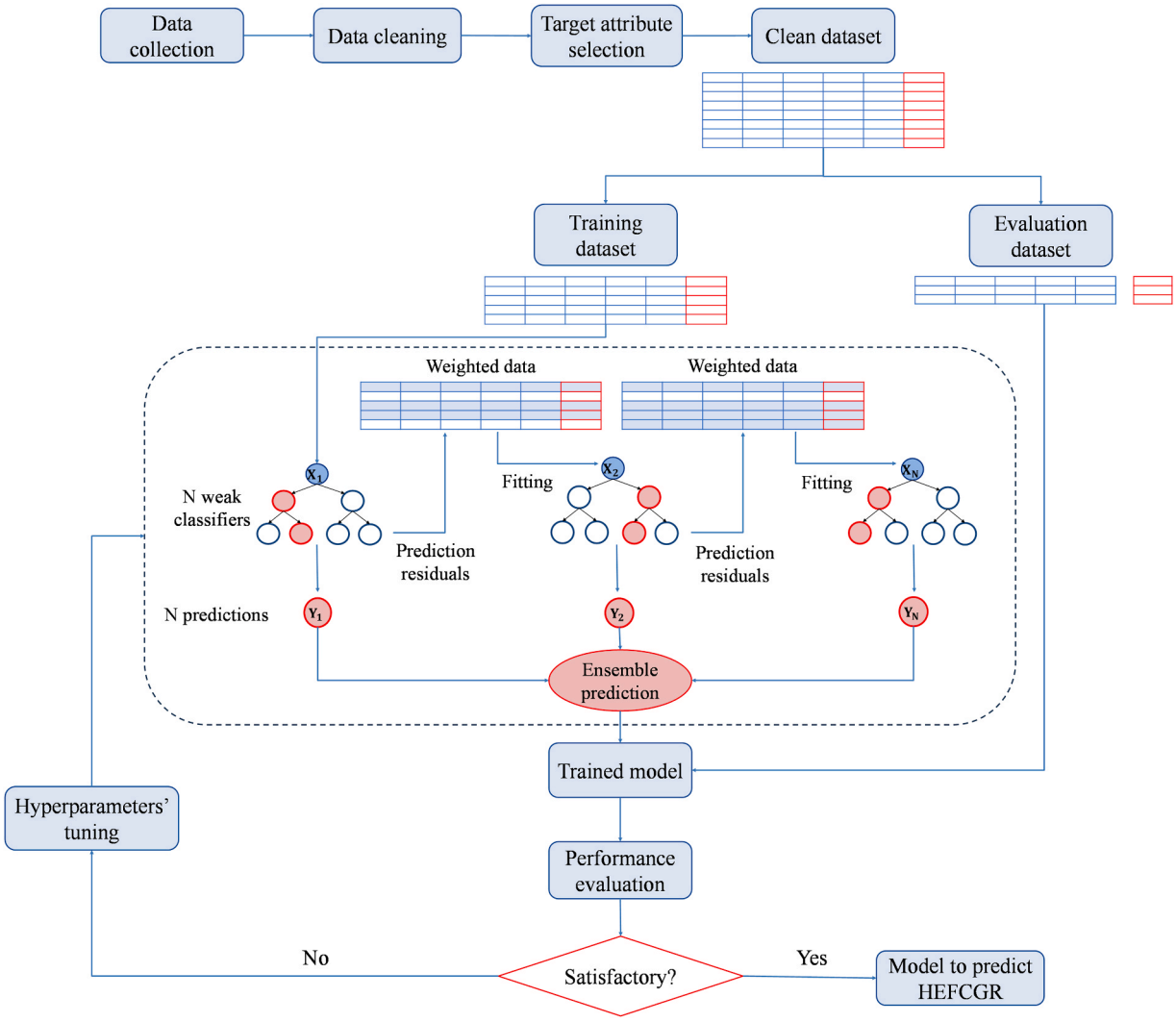

Fig. 1. Development of an ML classifier to predict the hydrogen effect on the FCGR.

repository collects the results of material tests in hydrogen environments with various carbon and low-alloy steels. The fatigue crack growth resistance is the only mechanical property considered in this study, but the tensile properties and fracture toughness can be predicted with a similar approach. The tests to quantify the per-cycle variation of the crack length (da/dN) were conducted according to the standard ASTM E647 (ASTM International, 2023). All the relevant testing conditions were specified, including the operating environment (i.e., pressure, temperature, hydrogen purity, and presence of inhibitors), the characteristics of the material (i.e., steel grade, chemical composition, microstructure, manufacturing technique, yield and tensile strengths, presence of welds), and the loading conditions (i.e., frequency, stress ratio, and stress intensity range).

The data are merged into a unique tabular repository, where each row indicates an FCGR test, and each column represents an attribute describing the testing conditions. Attributes presenting the same value for each test are removed from the database. In addition, attributes such as carbon (C), manganese (Mn), chromium (Cr), molybdenum (Mo), vanadium (V), nickel (Ni), and copper (Cu) contents are merged into a comprehensive feature. This parameter is known as carbon equivalent (CE) content and is calculated from Dearden-O'Neill's correlation in Eq. 4:

$$CE = \%C + \frac{\%Mn}{6} + \frac{\%Cr + \%Mo + \%V}{5} + \frac{\%Ni + \%Cu}{15} \quad (4)$$

Moreover, the testing environment is indicated as a comprehensive categorical feature. The reference environment has the nominal composition of the air (i.e., 78.08 % N_2, 20.95 % O_2, 0.93 % Ar, and 0.04 % CO_2), while hydrogen is present in two different purity grades. H_2 4.0 corresponds to $H_2 \geq 99.99$ %, $O_2 \leq 10$ ppm, and $H_2O \leq 20$ ppm, while H_2 5.0 corresponds to $H_2 \geq 99.999$ %, $O_2 \leq 2$ ppm, $H_2O \leq 3$ ppm, and $N_2 \leq 5$ ppm. Finally, if more than one test is reported under the same environmental and loading conditions, only the mean FCGR is considered and included in the database. Table 1 summarizes the features of the clean database and their range of variability.

3.2.2. *Target definition*

The target attribute should be a relevant parameter that quantifies the influence of H_2 environments on the fatigue crack growth acceleration. Hence, the HEFCGR measured in each test is compared to the reference value obtained in the air under the same loading conditions. An adimensional Fatigue Acceleration Factor is defined in Eq. 5:

$$FAF_{H_2} = \left.\frac{(da/dN)_{H_2}}{(da/dN)_{air}}\right|_{\Delta K,R=cost} \quad (5)$$

where $(da/dN)_{H_2}$ and $(da/dN)_{air}$ are the per-cycle variation of the crack length in pressurized hydrogen gas and air at ambient pressure, respectively, ΔK is the stress intensity range, and R is the stress ratio. Five severity classes are defined in Table 2 based on Fatigue

Table 1
Features of the clean database and corresponding ranges of variability.

Feature	Unit	Parameter	Type	Range of variability
Steel grade	-	Material	Categorical	API 5 L X42, API 5 L X60, API 5 L X80, AISI 4130
Carbon equivalent	%	Material	Numerical	0.278 – 0.615
Microstructure	-	Material	Categorical	Acicular ferrite, Banded ferrite, Polygonal ferrite, Pearlite, Tempered martensite
Yield strength	MPa	Material	Numerical	366 – 607
Ultimate tensile strength	MPa	Material	Numerical	486 – 950
Hydrogen pressure	MPa	Environmental	Numerical	1 – 45
Environment type	-	Environmental	Categorical	Air, H_2 4.0, H_2 5.0
Stress ratio	-	Mechanical	Numerical	0.1 – 0.8
Frequency	Hz	Mechanical	Numerical	0.1 – 1.0
Stress intensity range	$MPa{\cdot}m^{1/2}$	Mechanical	Numerical	3.9 – 37.5

Table 2
Definition of the classes for the target attribute.

Severity class	Fatigue Acceleration Factor	Symbol
Negligible severity	$1 < FAF_{H_2} \leq 5$	NS
Low severity	$5 < FAF_{H_2} \leq 25$	LS
Medium severity	$25 < FAF_{H_2} \leq 50$	MS
High severity	$50 < FAF_{H_2} \leq 75$	HS
Extreme severity	$FAF_{H_2} > 75$	ES

Acceleration Factor ranges.

3.2.3. Training of the gradient boosting machine classifier

The clean database is divided into two sub-datasets: the training database, composed of 70 % of the samples, and the evaluation database, which comprehends the remaining 30 %. The training dataset $\{(x_1, y_1), \ldots, (x_n, y_n)\}$ is composed of $(x_1, \ldots, x_n)$ independent variables (i.e., the features) and $(y_1, \ldots, y_n)$ dependent variables (i.e., the target) and is used to train a gradient boosting machine (GBM) classifier. This ensemble learning algorithm combines multiple weak learners (i.e., decision trees characterized by high error rates) to build an accurate and robust predictive model iteratively. The model starts with a simple base learner $F_0(x)$, which makes predictions based on the input data. At each iteration m, the algorithm calculates the residuals (i.e., errors), as per Eq. 6:

$$r_i^{(m)} = y_i - \hat{y}_i^{(m-1)} \tag{6}$$

where y_i is the actual label and $\hat{y}_i^{(m-1)}$ is the predicted label's probability from the model at iteration $m-1$. Then, a new tree $h_m(x)$ is trained to predict these residuals and added to the previous model $F_{m-1}(x)$. The updated model is given by Eq. 7:

$$F_m(x) = F_{m-1}(x) + \alpha{\cdot}h_m(x) \tag{7}$$

where α is the learning rate, which scales the contribution of each decision tree to control the learning process. The process of iteratively adding trees to the model, each one correcting the errors of the previous ones, is known as gradient boosting and is repeated for a specified number of iterations (Mason et al., 1999). At the end of this process, the model's prediction $\hat{y}$ is obtained by applying the sigmoid function to the final model $F_M(x)$ and converting the output of the model into a probability, as per Eq. 8:

$$\hat{y} = \sigma(F_M(x)) = \frac{1}{1 + e^{-F_M(x)}} \tag{8}$$

where σ indicates the sigmoid function.

The resulting GBM classifier has superior predictive capabilities and is more robust to outliers than other tree-based algorithms (i.e., decision tree or random forest). Its sequential construction, with each new tree correcting the errors of the previous ones, enhances performance and diminishes the influence of extreme values over time. It can grasp complex data patterns and nonlinear correlations without extensive data preprocessing. Furthermore, it achieves a good trade-off between the assumptions made to facilitate the learning process (i.e., the bias) and the sensitivity to small fluctuations in the training data (i.e., the variance). Like other tree-based algorithms, GBM provides insights into feature importance, aiding in feature selection and providing a clear understanding of how the model makes predictions. It also incorporates regularization techniques (e.g., controlling the learning rate and tree complexity) to prevent the model from closely fitting the training data but compromising the performance on new, unseen data. However, while a GBM classifier can outperform decision tree and random forest classifiers, it requires more careful hyperparameter tuning and is more computationally intensive (Friedman, 2001).

3.2.4. Evaluation of the model

The trained GBM classifier is fed with the evaluation dataset's unlabeled data. The predicted labels are compared with the true ones to quantify the share of correct predictions. Three evaluation metrics, namely Accuracy (in Eq. 9), Precision (in Eq. 10), and Recall (in Eq. 11), are used to assess the model's performance.

$$\text{Accuracy} = \frac{TP + TN}{TP + TN + FP + FN} \tag{9}$$

$$\text{Precision} = \frac{TP}{TP + FP} \tag{10}$$

$$\text{Recall} = \frac{TP}{TP + FN} \tag{11}$$

where TP and TN represent the true positive and true negative predictions, while FP and FN are the false positive and false negative ones. Accuracy indicates the share of labels correctly predicted, Precision is the fraction of correct positive predictions, and Recall is the share of TP labels correctly predicted (Brink et al., 2016). Instead of considering Accuracy, Precision, and Recall as separate metrics, the two latter can be combined into a unique evaluation parameter named F-score (F_β), defined in Eq. 12 (Chinchor, 1992):

$$F_\beta = (1 + \beta^2){\cdot}\frac{\text{Precision}{\cdot}\text{Recall}}{(\beta^2{\cdot}\text{Precision}) + \text{Recall}} \tag{12}$$

where β is a non-negative weight. If $\beta > 1$, the F-score prioritizes Recall; if $\beta < 1$, it prioritizes Precision; if $\beta = 1$, the F-score is the harmonic mean of Precision and Recall (Sasaki, 2007).

The classification model defines a probability that a set of features corresponds to one or another label. In the case of multiclass classifications, each probability vector is converted into a label based on a decision threshold. This parameter can be adjusted to optimize an evaluation metric. Lowering the threshold will increase the number of positive predictions and reduce the number of FN, optimizing the Recall. In contrast, raising the threshold will reduce the number of positive predictions, thus increasing the Precision (Goodfellow et al., 2016). Modifying the decision threshold allows for improving one metric at the expense of another but is unlikely to optimize both. The Precision-Recall (PR) curve plots the two metrics for each decision threshold. The Area Under the Curve PR (AUC PR) indicates the performance of the

classification model; a large AUC PR corresponds to high Recall and Precision (Murphy, 2012).

3.2.5. Optimization of the model

The hyperparameters of the GBM model are tuned through grid search to improve the model's performance and generalization capability. This method involves searching for the optimal combination in a specified hyperparameter space. The bounds and discretization are manually defined, and the GBM model is trained and evaluated with each set of parameters. Then, the optimization algorithm indicates the combination of hyperparameters that maximizes the model's Accuracy (James et al., 2023). Considering the characteristics of the GBM classifier, various hyperparameters can be tuned to optimize the performance. The number of estimators (*n_estimators*) indicates the number of decision trees to be created. Moreover, each tree is defined by the maximum number of levels (*max_depth*), the minimum number of samples required to split an internal node (*min_sample_split*), the minimum number of samples that could be in a leaf node (*min_samples_leaf*), and the maximum number of features to consider when looking for the best split (*max_features*). The *criterion* parameter indicates the function measuring the quality of a split. In addition, the *subsample* parameter defines the fraction of samples used to fit each base learner, while the *learning_rate* establish how much of the prediction error each base learner is allowed to correct. The loss function (*loss*) indicates the differentiable function that should be optimized in the trained model. Other hyperparameters, such as *n_iter_no_change*, *tol*, and *validation_fraction*, interrupt the learning process when the model can generalize to unseen data (Scikit-learn, 2024).

The feature selection process, which involves finding the set of features that best describes the phenomenon of hydrogen-enhanced fatigue and optimizes the performance of the GBM classifier, is crucial. It is performed by determining the feature importance and conducting a feature correlation analysis. The importance measures the average impurity decrease determined by a feature's split. If the feature is useful, it splits mixed-labeled nodes into more homogeneously labeled nodes. In contrast, splitting by low-importance features does not change nodes' purities. The correlation measures the linear relationship between two or more features. Independent variables with high correlation are more linearly dependent. Therefore, they have a similar influence on the dependent variable, and it is possible to predict one from the other. The most important features should be highly correlated with the target attribute and uncorrelated among themselves. The strength of the correlation between two numerical features is measured through the Pearson's coefficient, while the Cramér's V coefficient indicates association between two categorical features. The value of these coefficients ranges from −1 to 1, where −1 indicates a perfect negative linear relationship, 1 perfect positive linear relationship, and 0 specifies that there is no relationship between two features (Wang et al., 2017). If two or more features of the clean database are highly correlated, only that with the highest correlation with the target is included in the optimized model.

3.3. HyRIS methodology

The novel HyRIS methodology (*Risk-based Inspection Strategy for Hydrogen technologies*) results from the integration of the RBI approach with the predictions of the Fatigue Acceleration Factor in hydrogen environments. It can be divided into nine steps:

1. Definition of the case study and data collection;
2. Prediction of the FAF_{H_2} with the ML model;
3. Correction of the base damage factor for mechanical fatigue;
4. Calculation of the probability of failure;
5. Calculation of the consequence of failure;
6. Calculation of the risk;
7. Development of a risk-based ranking;
8. Development of the inspection plan;
9. Reassessment of the inspection plan.

First, three real-world pipelines are selected as a case study. A comprehensive set of data is gathered, including information regarding the geometry, material, design characteristics, operating conditions, and inspection history. These pipelines have been used for natural gas transport and are assessed for being repurposed for H_2 transport. The same operating conditions are assumed for natural gas, hydrogen, and a natural gas-hydrogen blend. While the conventional RBI methodology allows for calculating most damage factors, the D_f for mechanical fatigue must be corrected to consider the effect of H_2 environments. Therefore, the FAF_{H_2} is predicted through the GBM classifier for each pipeline leg, depending on the characteristics of the material and the operating conditions, and combined with the damage factor for mechanical fatigue (D_f^{fat}), as per Eq. 13:

$$D_f^{HEF} = D_f^{fat} \cdot FAF_{H_2} \tag{13}$$

where D_f^{fat} is calculated according to API RP 581 (American Petroleum Institute, 2019). Notably, the FAF_{H_2} can increase the base damage factor 5, 25, 50, 75, or 100-fold, depending on the classifier's prediction. Then, the failure probabilities are calculated by combining all the damage factors with the generic failure frequencies and management system factors (as per Eq. 1). The consequences of failure are evaluated based on the operating conditions of the pipelines, the fluids' properties, and the mitigation systems in place. Then, probabilities and consequences are combined to calculate the risk, and the various pipeline legs are ranked. It is possible to develop an inspection plan to keep the probability of failure below a defined acceptance threshold, prioritizing the high-risk components. In-line inspections can be conducted with intelligent pigs composed of multiple linked modules, each carrying the instrumentation to measure a specific parameter. These activities are crucial to obtain more precise information about the pipelines' conditions. The new data available can be used to update and reassess the inspection plan, reducing the uncertainty and allowing a more precise evaluation of the probabilities of failure. Fig. 2 describes the main steps of the HyRIS methodology. The conventional RBI s represented with dot-dashed lines (in blue blocks), the ML-aided prediction of the hydrogen effect on mechanical fatigue is marked with dashed lines (in red blocks), and the integration of RBI and ML is indicated with solid lines (in purple blocks).

4. Case study

This section presents the case study to validate the HyRIS methodology. Three Norwegian natural gas pipelines are assessed for repurposing for hydrogen transport. All these pipelines (hereafter named S, L, and N) are onshore and aboveground. The pipeline S has been used for natural gas transport for 39 years. It is made of vintage API 5 L X65 steel with a banded microstructure; it was rolled and formed through the UOE method. This manufacturing process involves cold forming (where the plate edges are formed in the "U" and "O" press), longitudinal welding, and finally expansion (Toscano et al., 2008). The pipeline L, operational since 2006, is made of API 5 L X60 steel with a polygonal ferritic and pearlitic microstructure. It was rolled, formed, and longitudinally welded using the same method as pipeline S. A new pipeline is also considered. Similarly to pipeline S, pipeline N is made of X65 steel but has undergone a different manufacturing process (i.e., seamless extrusion), resulting in a fine-grained ferrite and bainite microstructure. The geometrical characteristics and structural materials of the pipelines are summarized in Table 3.

The pipelines are assumed to transport natural gas (NG), hydrogen (H_2), or a blend of 90 $\%_{vol}$ natural gas and 10 $\%_{vol}$ hydrogen (NG-H_2). The network operator gives the nominal pressure for each pipeline, while the temperature is the region's annual average. The amplitudes and frequencies of the pressure fluctuations refer to natural gas

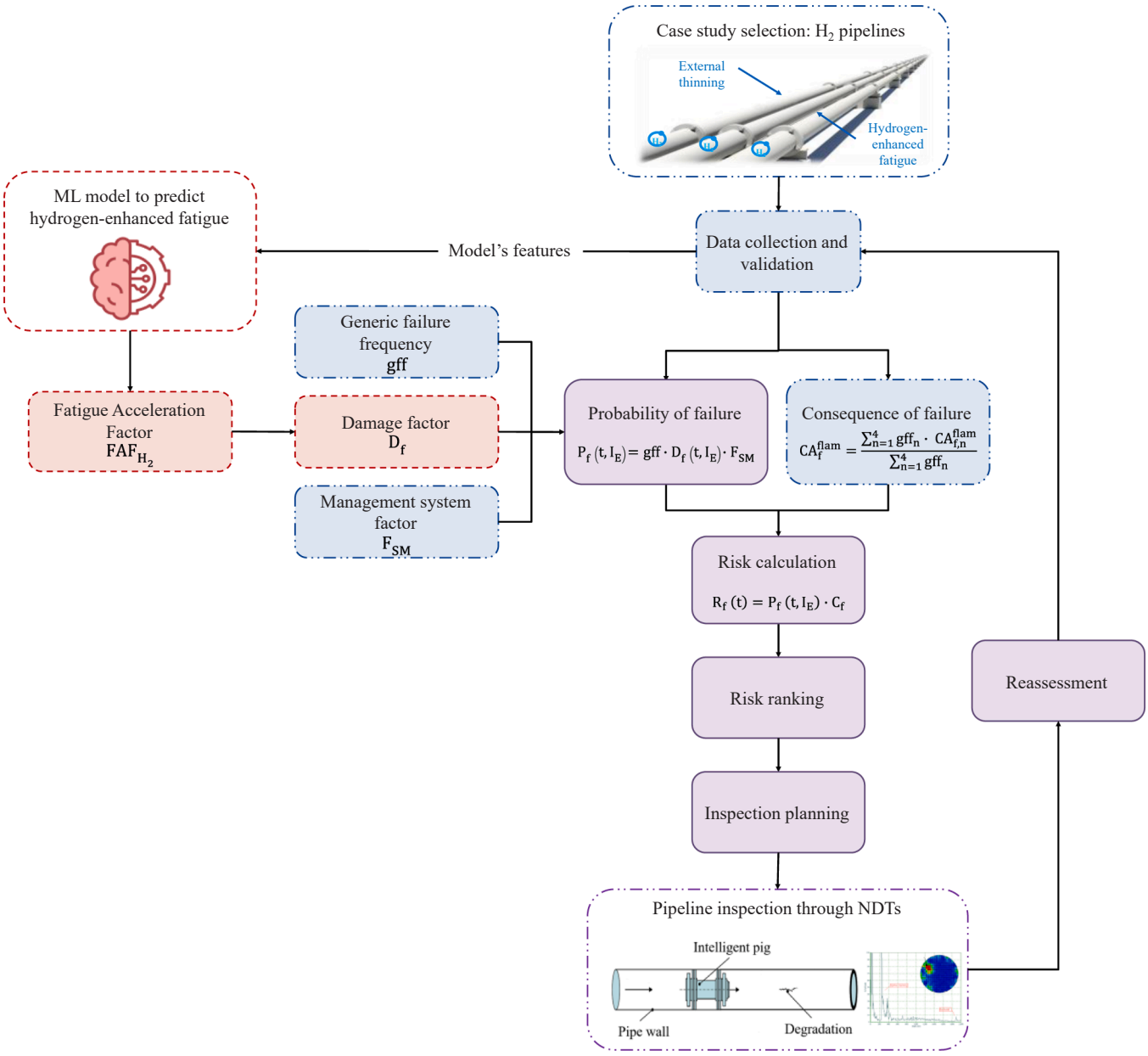

Fig. 2. Flow diagram of the HyRIS methodology.

Table 3
Technical characteristics of the pipelines (Alvaro et al., 2021).

	Pipeline S	Pipeline L	Pipeline N
Start service date	01.01.1985	01.01.2006	01.01.2019
Wall thickness	26 mm	41 mm	15.4 mm
Outer diameter	770 mm	1100 mm	321 mm
Length	100 m	100 m	100 m
Type	UOE, longitudinally welded	UOE, longitudinally welded	Extruded, seamless
Material	API 5 L X65	API 5 L X60	API 5 L X65
Microstructure	Banded ferrite, pearlite	Polygonal ferrite, pearlite	Acicular ferrite, bainite
Carbon equivalent	0.48 %	0.42 %	0.35 %
Yield strength	526 MPa	481 MPa	543 MPa
Ultimate tensile strength	627 MPa	604 MPa	610 MPa

transport, but the same values are assumed for pipelines carrying H_2 or NG-H_2 blends. Three scenarios can be defined: underload, mean load, and overload. These types of pressure fluctuations depend on the location along the pipeline. Underload-type loads are characterized by mean pressure close to the design limit, only allowing fluctuations towards lower pressure levels. A few significant pressure fluctuations are followed by frequent minor cycles. This load type is typically observed downstream of the compression stations. Mean loads are common further down from the compressor, where the average pressure is lower. Pressure peaks and pressure drops are frequent, even if the amplitude of these fluctuations is limited. Overload-type fluctuations can be observed close to the suction sites and are characterized by pressure pikes above the mean value. The mean pressure is much lower than underload-type fluctuations; hence, these conditions are less severe for fatigue crack growth than the previous ones (Zhao et al., 2016). The loading conditions of three pipe legs are summarized in Table 4 for each pipeline.

The technical characteristics of the pipelines include the material-related features of the ML model (i.e., steel grade, carbon equivalent

Table 4
Operating conditions of the pipelines downstream of the compressor (DC), along the pipe (P), and close to the suction site (SS).

Pipeline leg	Average temperature [°C]	Nominal pressure [MPa]	Minimum pressure [MPa]	Maximum pressure [MPa]	Frequency [Hz]
S-DC	7	14.0	7.0	15.0	10^{-6}
			13.7	14.3	1
S-P	7	11.0	8.0	14.0	$5{\cdot}10^{-5}$
			10.8	11.2	$5{\cdot}10^{-1}$
S-SS	7	8.0	7.0	11.0	10^{-5}
			7.9	8.1	10^{-1}
L-DC	7	20.0	11.0	21.0	10^{-6}
			19.7	20.3	1
L-P	7	15.0	11.5	18.5	$5{\cdot}10^{-5}$
			14.8	15.2	$5{\cdot}10^{-1}$
L-SS	7	10.0	8.5	14.0	10^{-5}
			9.9	10.1	10^{-1}
N-DC	7	10.0	6.0	11.0	10^{-6}
			9.6	10.4	1
N-P	7	7.0	5.0	9.0	$5{\cdot}10^{-5}$
			6.7	7.3	$5{\cdot}10^{-1}$
N-SS	7	5.0	4.0	7.5	10^{-5}
			4.8	5.2	10^{-1}

content, microstructure, yield strength, and ultimate tensile strength). The gas composition is measured at the inlet and outlet of the pipeline to ensure that the fuel meets quality standards and safety requirements. The pressure is continuously monitored to detect any leaks or blockages. Fourier's analysis of pressure fluctuations allows the decomposition of complex pressure signals into simpler sinusoidal components, determining their amplitude and frequency (Howell, 2017). These parameters can be monitored online with sensors and transmitters. Considering that load cycles in pipeline systems result from pressure fluctuations, the stress ratio can be expressed as the ratio between minimum and maximum operating pressures, as per Eq. 14:

$$R = \frac{p_{min}}{p_{max}} \tag{14}$$

On the other hand, the stress intensity range depends on the pipeline's geometry, the size of pre-existing cracks, and the difference between maximum and minimum pressure. In the case of an axially oriented crack with a semielliptical shape on the inner surface of a cylinder, the stress intensity range can be determined through Eq. 15, according to the standard API 579 (American Petroleum Institute, 2016b) for the crack geometry type KCSCLE1:

$$\Delta K = \frac{D_o}{2t}\cdot\beta\cdot\sqrt{\pi a}\cdot(p_{max} - p_{min}) \tag{15}$$

where D_o and t (m) indicate the outer diameter and thickness of the pipeline, β is the geometry factor, a (m) is the crack depth, and p_{max} and p_{min} (MPa) are the maximum and minimum internal pressures. The crack depth can be determined through NDTs, such as acoustic emission and ultrasonic testing. Nevertheless, at the first iteration it should be assumed. The typical initial crack depth and semi-length values are 2 mm and 3 mm, respectively (ASME International, 2019). The crack size can be adjusted based on the age of the component and the results of previous inspections. As a result, the HyRIS methodology, while initially leading to high uncertainty, becomes more accurate after each inspection, allowing for a more precise prediction of future degradation rates.

5. Results and discussion

This section delves into applying and validating the HyRIS methodology on three pipelines carrying natural gas, hydrogen, or hydrogen blended with natural gas. Section 5.1 summarizes the features and hyperparameters of the optimized machine-learning model. In addition, it presents the performance of the GBM classifier, including the evaluation metrics, confusion matrix, and PR curves. Section 5.2 is dedicated to the risk-based inspection of the pipelines, presenting the probabilities and consequences of failure, the risk-based ranking, and the inspection plan. This section highlights the differences between hydrogen and natural gas, discussing the implications of H_2 transport on pipelines' degradation.

5.1. Performance of the machine-learning model

The clean database comprises features associated with the materials' characteristics, operating environment, and mechanical load. The importance of each feature indicates its relative significance in predicting the FAF_{H_2}. As shown in Fig. 3, the loading conditions significantly impact the hydrogen-induced fatigue acceleration. The stress intensity range depends on the pipeline's geometry, pressure fluctuations' amplitude, and pre-existing cracks' size and shape. This comprehensive parameter is crucial for the FAF_{H_2} and defines the crack propagation regimes. In addition, the stress intensity ratio depends on the maximum and minimum pressures and contributes to determining the amplitude of pressure cycles. As hydrogen-induced damages are time-dependent phenomena, the frequency of pressure fluctuations notably impacts the FCGR acceleration. H_2 partial pressure is the only environmental parameter considered, but it is the driving force for the hydrogen uptake. The steel grade, indicated by the specification API 5 L (American Petroleum Institute, 2018), is the most important material parameter and establishes the steel's nominal chemical composition and minimum strength. As a result, CE content, yield strength (YS), and ultimate tensile strength (UTS) slightly influence the model's predictions. The experimental evidence confirms that the strength-dependency of the HEFCGR is negligible (Tau et al., 1996). On the other hand, the material's microstructure is a crucial feature. Depending on the manufacturing process, steels with the same grade may have significantly different microstructures. Acicular, banded, and polygonal ferrites have different hydrogen diffusivity and responses to load cycles in H_2 environments.

The correlation matrix in Fig. 4 can help us understand the feature-feature and feature-target relationships. Theoretically, if two features have a high correlation, one can be inferred from the other and eliminated. Most material properties are highly correlated, particularly steel grade with microstructure or carbon equivalent and yield strength with ultimate tensile strength. This is reasonable since steels with the same grade have an almost identical composition and a narrow range of YS and UTS. In contrast, loading parameters (i.e., stress intensity range, stress ratio, and frequency) are independent of the other features and have low correlation coefficients. The hydrogen pressure seems highly correlated with YS and UTS, but this relationship does not result from any meaningful connection and can be considered spurious. The correlation between FAF_{H_2} and features is coherent with the feature importance in Fig. 3.

Therefore, the features of the optimized model can be selected by combining importance and correlation, iteratively training the model, and evaluating its performance with different subsets of features. Once the best-performing set of features is selected, the hyperparameters can be tuned through grid search. Table 5 summarizes the features and hyperparameters of the optimized model. Carbon equivalent content and ultimate tensile strength are eliminated since they have the lowest importance and high correlation coefficients, thus obtaining an optimized model with seven features. The tuned hyperparameters ensure a satisfactory trade-off between accuracy and generalization capability. On the one hand, the low learning rate, the limit on the tree depth, and the impurity decrease threshold prevent overfitting. Conversely, the low values of the minimum number of samples in internal and leaf nodes and the large number of estimators increase the model's accuracy.

The model optimization allows us to obtain a GBM classifier with good performance on the evaluation dataset and satisfactory generalization capability on unseen data. Table 6 reports the Accuracy of the

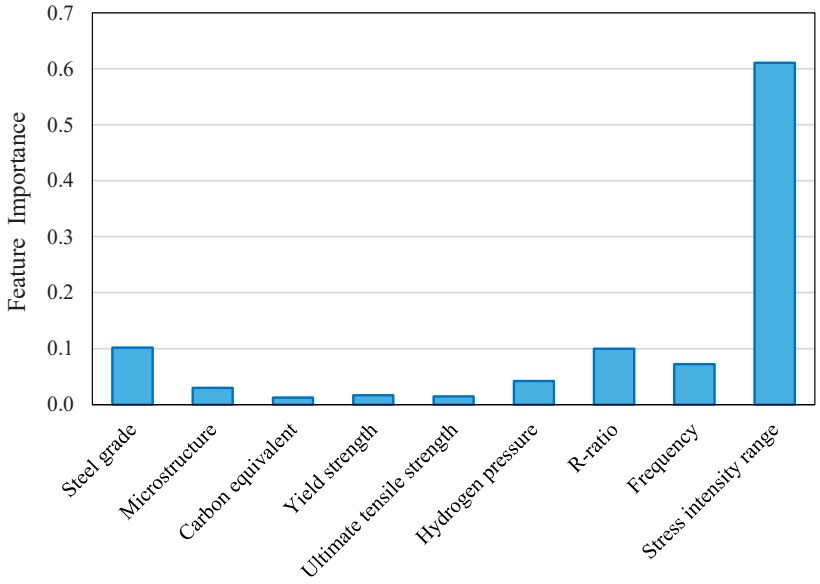

Fig. 3. Importance of the features in the clean database.

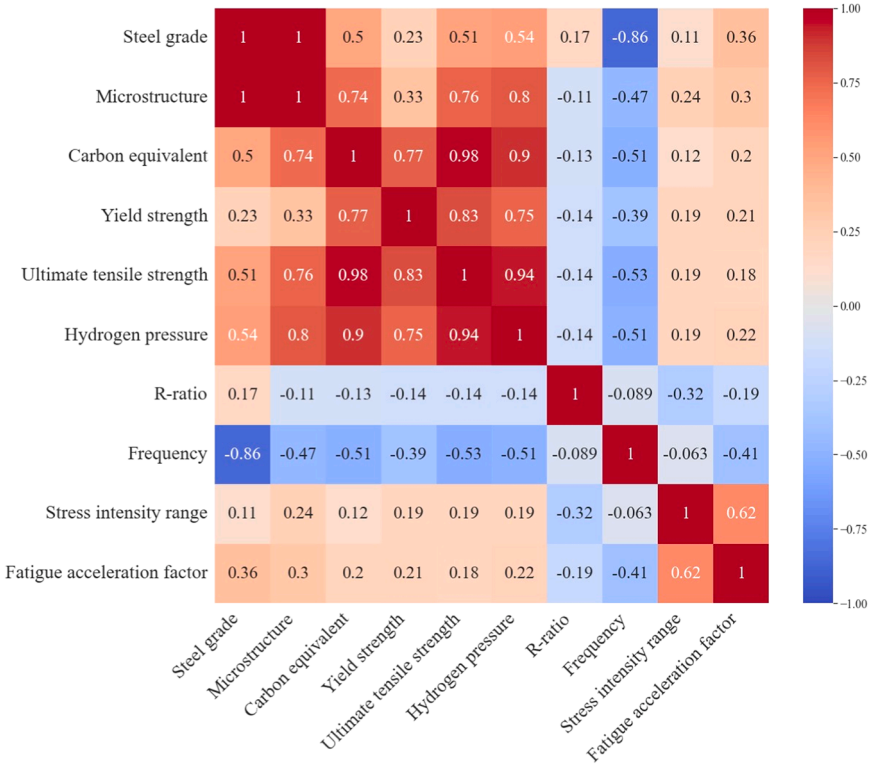

Fig. 4. Correlation matrix for the features and target of the clean database.

optimized model and the Precision, Recall, AUC PR, and F_1-score for each target attribute.

Fig. 5 shows the confusion matrix. The x-axis and the y-axis indicate the predicted and actual labels, respectively. Hence, the numbers on the main diagonal represent the correct predictions, the numbers above the main diagonal are the overestimated predictions, and the numbers below are the underestimated ones. Considering only the mis-predictions, the closer they are to the main diagonal, the lower the difference between actual and predicted labels.

The model is 94.61 % accurate and can successfully predict the severity of the hydrogen-enhanced fatigue crack growth. The predictions of negligible, low, and medium severity labels are characterized by high Precision (from 96.46 % to 96.77 %), Recall (from 95.61 % to 99.16 %), and AUC PR (from 96.72 % to 99.68 %). Most of the labels incorrectly predicted have an FAF_{H_2} near the negligible-low or low-medium severity thresholds. Conversely, the lower effectiveness of the GBM classifier in predicting high and extreme severity labels is primarily due to the unbalanced dataset. Moreover, the relationships between features and labels become increasingly complex at higher ΔK, where the FCGR in compressed hydrogen gas significantly deviates from that in the air. The higher complexity of the phenomenon, combined with the limited number of data to learn from, leads to lower Precision (i.e.,

Table 5
Features and hyperparameters of the optimized GBM classifier.

Feature	Symbol
Steel grade	SGr
Microstructure	Ms
Yield strength	YS
Hydrogen pressure	p
Stress ratio	R
Frequency	f
Stress intensity range	ΔK
Hyperparameter	**Selected value**
loss	log_loss
learning_rate	0.01
subsample	1.0
criterion	friedman_mse
validation_fraction	0.1
n_estimators	1100
min_sample_split	2
min_sample_leaf	1
max_depth	6
min_impurity_decrease	0.01
max_features	sqrt

Table 6
Evaluation metrics of the GBM classifier.

Target attribute	Accuracy	Precision	Recall	AUC PR	F_1-score
Negligible severity	0.9461	0.9677	0.9677	0.9968	0.9677
Low severity	0.9461	0.9672	0.9916	0.9925	0.9793
Medium severity	0.9461	0.9646	0.9561	0.9672	0.9604
High severity	0.9461	0.8235	0.6667	0.8782	0.7368
Extreme severity	0.9461	0.7143	0.8333	0.8200	0.7692

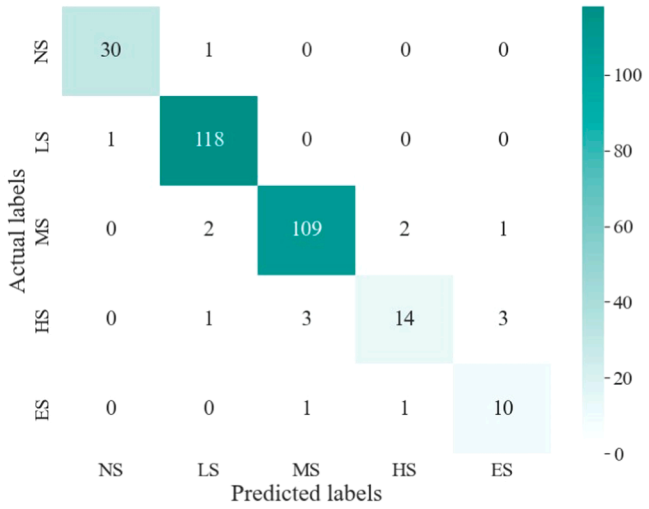

Fig. 5. Confusion matrix for the GBM classifier.

82.35 % and 71.43 %, respectively), Recall (i.e., 66.67 % and 83.33 %, respectively), and AUC PR (i.e., 87.82 % and 82.00 %, respectively). Notably, two severity labels are significantly underestimated, resulting in incorrect predictions and potentially critical errors in the risk assessment. Fig. 6 shows the Precision-Recall curves for each severity class, confirming the evaluation metrics in Table 6 and the confusion matrix in Fig. 5. While finding a good trade-off between Precision and Recall is easy for negligible, low, and medium severities, the decision threshold should be carefully selected for high and extreme labels. In this case, a high Recall is preferable since it is acceptable that the model eventually generates false positives rather than misses high and extreme severities. This error could determine an underestimation of the

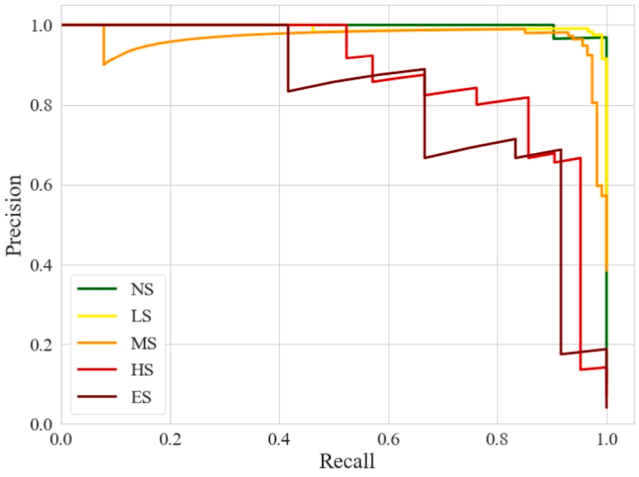

Fig. 6. Precision-Recall curve for each class of the GBM classifier.

degradation rate in hydrogen environments and, consequently, an actual risk of failure higher than expected.

5.2. Risk-based inspection

The first and second evaluation dates for the risk-based inspection are set for the 1st of January 2024 and the 1st of January 2029. These dates align with the American Petroleum Institute's recommendation of a five-year inspection interval for pipelines carrying flammable substances (American Petroleum Institute, 2024). By quantifying the risk at the scheduled inspection date, it is possible to determine whether the conventional time-based inspection strategy is over- or under-conservative. The RBI approach is adopted considering the same pipelines used for natural gas, hydrogen, and a blend of natural gas and 10 $\%_{vol}$ hydrogen to demonstrate how the transported substance influences the probabilities and consequences of failure. Considering the pipelines' design, operating environment, and loading conditions, two damage mechanisms are likely to occur, i.e., external corrosion and mechanical fatigue.

All the pipelines are onshore and aboveground and exposed to external thinning damage (Abubakirov et al., 2020). A fusion-bonded epoxy coating protects the outer surface from atmospheric agents, but the coating condition and quality depend on the start service date. Pipeline S has a medium-quality and heavily damaged coating, while pipeline L is slightly damaged. In contrast, a high-quality coating without any visible damage protects pipeline N. Moreover, line packing exposes all the pipelines to daily pressure fluctuations. Table 7 reports the generic failure frequencies, management system factors, and damage factors for each active degradation mechanism at the first and second evaluation dates. The probabilities of failure are calculated by combining the abovementioned factors.

Regardless of the substance transported, the severely damaged coating exposes pipeline S to atmospheric corrosion. The working conditions are particularly critical downstream of the compressor, where there is the highest pressure, and the pipeline operates near its design limit. While mechanical fatigue is negligible in natural gas environments, the combined effect of cyclic underloads at low frequency, susceptible microstructure, and elevated nominal pressure accelerates the FCGR in hydrogen environments up to 25-fold. In contrast, the other pipeline legs are negligibly susceptible to hydrogen-enhanced fatigue due to the lower average pressure, lower amplitude of pressure fluctuations, and higher frequency. In the case of NG-H_2 blend, the hydrogen partial pressure is ten times lower. Nevertheless, the hoop stress induced by the pressure fluctuations is proportional to the total pressure and, therefore, is the same. As a result, even if the FCGR is most likely lower

Table 7
Generic failure frequency, management system factor, damage factors, and probabilities of failure.

ID	Substance	gff	F_{SM}	$D_f^{corr}(t_0)$	$D_f^{corr}(t)$	D_f^{fat}	FAF_{H_2}	D_f^{HEF}	$P_f(t_0)$	$P_f(t)$
S-DC	Natural gas	$3.06 \cdot 10^{-5}$	0.25	91.51	122.31	4.00	-	-	$7.34 \cdot 10^{-4}$	$9.71 \cdot 10^{-4}$
S-P	Natural gas	$3.06 \cdot 10^{-5}$	0.25	55.90	74.93	4.00	-	-	$4.60 \cdot 10^{-4}$	$6.07 \cdot 10^{-4}$
S-SS	Natural gas	$3.06 \cdot 10^{-5}$	0.25	10.55	13.95	4.00	-	-	$1.12 \cdot 10^{-4}$	$1.38 \cdot 10^{-4}$
L-DC	Natural gas	$3.06 \cdot 10^{-5}$	0.25	548.88	643.45	4.00	-	-	$4.25 \cdot 10^{-3}$	$4.98 \cdot 10^{-3}$
L-P	Natural gas	$3.06 \cdot 10^{-5}$	0.25	324.83	384.08	4.00	-	-	$2.53 \cdot 10^{-3}$	$2.98 \cdot 10^{-3}$
L-SS	Natural gas	$3.06 \cdot 10^{-5}$	0.25	45.32	54.06	4.00	-	-	$3.79 \cdot 10^{-4}$	$4.46 \cdot 10^{-4}$
N-DC	Natural gas	$3.06 \cdot 10^{-5}$	0.25	1.87	1.87	2.00	-	-	$2.97 \cdot 10^{-5}$	$2.97 \cdot 10^{-5}$
N-P	Natural gas	$3.06 \cdot 10^{-5}$	0.25	1.87	1.87	2.00	-	-	$2.97 \cdot 10^{-5}$	$2.97 \cdot 10^{-5}$
N-SS	Natural gas	$3.06 \cdot 10^{-5}$	0.25	1.87	1.87	2.00	-	-	$2.97 \cdot 10^{-5}$	$2.97 \cdot 10^{-5}$
S-DC	Natural gas + 10 $\%_{vol}$ Hydrogen	$3.06 \cdot 10^{-5}$	0.25	91.51	122.31	-	LS	100.00	$1.47 \cdot 10^{-3}$	$1.71 \cdot 10^{-3}$
S-P	Natural gas + 10 $\%_{vol}$ Hydrogen	$3.06 \cdot 10^{-5}$	0.25	55.90	74.93	-	NS	20.00	$5.83 \cdot 10^{-4}$	$7.30 \cdot 10^{-4}$
S-SS	Natural gas + 10 $\%_{vol}$ Hydrogen	$3.06 \cdot 10^{-5}$	0.25	10.55	13.95	-	NS	20.00	$2.35 \cdot 10^{-4}$	$2.61 \cdot 10^{-4}$
L-DC	Natural gas + 10 $\%_{vol}$ Hydrogen	$3.06 \cdot 10^{-5}$	0.25	548.88	643.45	-	LS	100.00	$4.99 \cdot 10^{-3}$	$5.71 \cdot 10^{-3}$
L-P	Natural gas + 10 $\%_{vol}$ Hydrogen	$3.06 \cdot 10^{-5}$	0.25	324.83	384.08	-	NS	20.00	$2.65 \cdot 10^{-3}$	$3.11 \cdot 10^{-3}$
L-SS	Natural gas + 10 $\%_{vol}$ Hydrogen	$3.06 \cdot 10^{-5}$	0.25	45.32	54.06	-	NS	20.00	$5.02 \cdot 10^{-4}$	$5.69 \cdot 10^{-4}$
N-DC	Natural gas + 10 $\%_{vol}$ Hydrogen	$3.06 \cdot 10^{-5}$	0.25	1.87	1.87	-	NS	10.00	$9.12 \cdot 10^{-5}$	$9.12 \cdot 10^{-5}$
N-P	Natural gas + 10 $\%_{vol}$ Hydrogen	$3.06 \cdot 10^{-5}$	0.25	1.87	1.87	-	NS	10.00	$9.12 \cdot 10^{-5}$	$9.12 \cdot 10^{-5}$
N-SS	Natural gas + 10 $\%_{vol}$ Hydrogen	$3.06 \cdot 10^{-5}$	0.25	1.87	1.87	-	NS	10.00	$9.12 \cdot 10^{-5}$	$9.12 \cdot 10^{-5}$
S-DC	Hydrogen	$3.06 \cdot 10^{-5}$	0.25	91.51	122.31	-	LS	100.00	$1.47 \cdot 10^{-3}$	$1.71 \cdot 10^{-3}$
S-P	Hydrogen	$3.06 \cdot 10^{-5}$	0.25	55.90	74.93	-	NS	20.00	$5.83 \cdot 10^{-4}$	$7.30 \cdot 10^{-4}$
S-SS	Hydrogen	$3.06 \cdot 10^{-5}$	0.25	10.55	13.95	-	NS	20.00	$2.35 \cdot 10^{-4}$	$2.61 \cdot 10^{-4}$
L-DC	Hydrogen	$3.06 \cdot 10^{-5}$	0.25	548.88	643.45	-	MS	200.00	$5.76 \cdot 10^{-3}$	$6.48 \cdot 10^{-3}$
L-P	Hydrogen	$3.06 \cdot 10^{-5}$	0.25	324.83	384.08	-	LS	100.00	$3.27 \cdot 10^{-3}$	$3.72 \cdot 10^{-3}$
L-SS	Hydrogen	$3.06 \cdot 10^{-5}$	0.25	45.32	54.06	-	NS	20.00	$5.02 \cdot 10^{-4}$	$5.69 \cdot 10^{-4}$
N-DC	Hydrogen	$3.06 \cdot 10^{-5}$	0.25	1.87	1.87	-	NS	10.00	$9.12 \cdot 10^{-5}$	$9.12 \cdot 10^{-5}$
N-P	Hydrogen	$3.06 \cdot 10^{-5}$	0.25	1.87	1.87	-	NS	10.00	$9.12 \cdot 10^{-5}$	$9.12 \cdot 10^{-5}$
N-SS	Hydrogen	$3.06 \cdot 10^{-5}$	0.25	1.87	1.87	-	NS	10.00	$9.12 \cdot 10^{-5}$	$9.12 \cdot 10^{-5}$

than in pure hydrogen gas, the severity classes (associated with a FAF_{H_2} range) appear identical. The minor pressure cycles with high frequency and low amplitude result in a stress intensity range below 1.1 MPa $\cdot$ $m^{1/2}$ (i.e., the threshold defined in ASME B31.12) and, therefore, do not influence the fatigue crack propagation.

Similar considerations apply to the pipeline L. The slightly damaged coating and high operating pressure make this pipeline extremely susceptible to external corrosion. In addition, the damage factor tends to increase over time, potentially compromising the components' integrity. Mechanical fatigue is not an issue in natural gas environments but increases up to 50-fold in hydrogen gas. As with pipeline S, the leg downstream of the compressors is the most affected by hydrogen-enhanced fatigue, while the susceptibility decreases moving toward the suction site. The FAF_{H_2} is lower for the hydrogen-natural gas blend. However, the severity of the underloads downstream of the compression station still determines a 25-fold increase in FCGR compared to natural gas. Overall, pipeline L is concurrently subjected to severe atmospheric corrosion and fatigue degradation and, therefore, has the highest probability of failure.

Finally, the undamaged high-quality coating makes pipeline N almost insensitive to corrosion. In addition, the corrosion rate does not increase over time. Mechanical fatigue slightly increases if the pipeline is exposed to pressurized hydrogen. Similarly to pipeline S, even if the FCGR should be lower in NG-H_2 blends than in hydrogen gas, the severity class is negligible in both cases. However, the 5-fold increase in the damage factor for mechanical fatigue is significantly conservative if pipeline N transports natural gas with 10 $\%_{vol}$ hydrogen.

The consequences of failure are evaluated by defining the thresholds for burn injuries (LaChance et al., 2011), corresponding to an overpressure of 14 kPa for explosions, thermal radiation of 12.5 kW/m^2 for fires, and fuel concentration equal to the low flammability limit in air for flash fires. The consequence area for each component is calculated as the

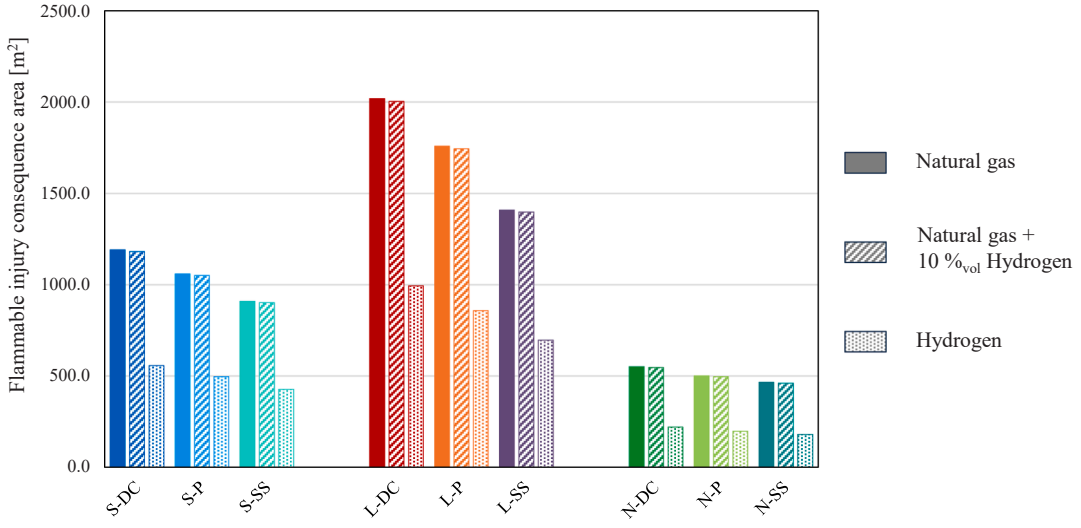

Fig. 7. Consequence areas for the pipelines carrying natural gas, natural gas - 10 $\%_{vol}$ hydrogen, and pure hydrogen.

average of the consequence areas of four hole sizes, weighted on their distribution probability. The results for each pipeline leg are summarized in Fig. 7 in the cases of transport of natural gas, natural gas blended with 10 $\%_{vol}$ hydrogen, and pure hydrogen.

The consequence areas depend on various factors. These include the type of flammable substance released, the amount of substance available for release, and the operating pressure of the component. The pipeline legs downstream of the compression stations, operating at higher pressures, have the highest consequences of failure. The other legs, particularly those near the suction sites, operate at lower pressures and, consequently, have lower consequence areas. Notably, all the pipeline legs have the same consequence areas for small, medium, and large holes (with diameters ranging from 6 to 101 mm) in the case of continuous releases. Small, medium, and large hydrogen releases have consequence areas of approximately 4, 59, and 956 m^2, respectively. For the same hole sizes, natural gas releases result in 10, 177, and 3270 m^2 consequence areas, while natural gas-hydrogen releases have slightly lower consequences (i.e., 10, 175, and 3236 m^2). This negligible difference is due to the low hydrogen content within the blend (10 $\%_{vol}$ corresponds to approximately 1.5 $\%_{wt}$).

When the gas flows under sonic conditions through a hole, the mass flow rate is choked and is not influenced by the upstream pressure. The choked flow depends on the gas density, and that of natural gas is ten to eleven times higher than hydrogen's at the same temperature and pressure (NIST, 2024). As a result, a significantly higher amount of natural gas can be released from a hole with a defined diameter. In addition, fires are the most likely scenario for ignited releases resulting from the loss of integrity of pipelines, and natural gas flames have higher radiative heat flux than hydrogen flames (Glassman et al., 2014). Therefore, the consequence areas for NG releases are approximately three times larger than those for H_2 releases. At the same time, essential differences between the three pipelines and various legs of the same pipeline can be observed for the full-bore ruptures. In this case, the consequence area is proportional to the fuel mass available for an instantaneous release. Since each leg of the same pipe has the same volume, the mass depends only on the gas density (i.e., pressure): higher near the compression station and lower near the suction site. Therefore, the consequences of instantaneous releases are directly proportional to the size and operating pressure of the pipeline leg considered.

By combining probabilities and consequences of failure, the risk for each pipeline leg (DC, P, and SS) can be calculated for each substance transported. Fig. 8 shows the iso-risk plot, where consequences and probabilities are on a logarithmic scale. The iso-risk lines are marked in green, yellow, orange, and red, and represent the thresholds between low, medium, medium-high, and high-risk zones.

The first leg of pipeline S is highly affected by atmospheric corrosion. The recommended inspection consists of visual testing (VT) on more than 95 % of the pipeline, followed by ultrasonic (UT) or radiographic testing (RT) on potentially damaged areas. This inspection should be conducted regardless of the substance transported. In contrast, the operating environment influences the magnitude of fatigue degradation: it is negligible for natural gas, but even small amounts of hydrogen can significantly increase the degradation rate. However, it is essential to note that the RBI methodology does not provide effective inspections for mechanical fatigue. Therefore, the failure probability can be reduced by modifying the operating conditions. The working conditions of the leg downstream of the compression station (S-DC) are appropriate for natural gas transport but result in excessive fatigue degradation in H_2 environments. In contrast, the legs S-P and S-SS are less affected by atmospheric corrosion and mechanical fatigue. As a result, the recommended inspection, i.e., visual testing on 30 % of the pipeline, eventually followed by UT or RT, can be postponed.

Considering the elevated P_f, inspecting pipeline L immediately and monitoring the potential risk of external thinning in the first two legs (i.e., L-DC and L-P) is crucial. The working conditions of pipeline L are suitable for natural gas transport but result in excessive fatigue degradation in H_2 environments. Therefore, the nominal pressure should be lowered, and the amplitude of pressure fluctuations reduced, particularly in the leg downstream of the compression station. The internal pressure of pipeline L (ranging from 20 to 10 MPa) is extremely elevated, and pipelines made of API 5 L X60 should not exceed the nominal pressure of 6 MPa, as per the standard ASME B31.12 (ASME International, 2019).

In contrast, external thinning slightly damages pipeline N and remains below the threshold at the second evaluation date. Therefore, a fairly effective inspection with visual testing on 30 % of the pipeline,

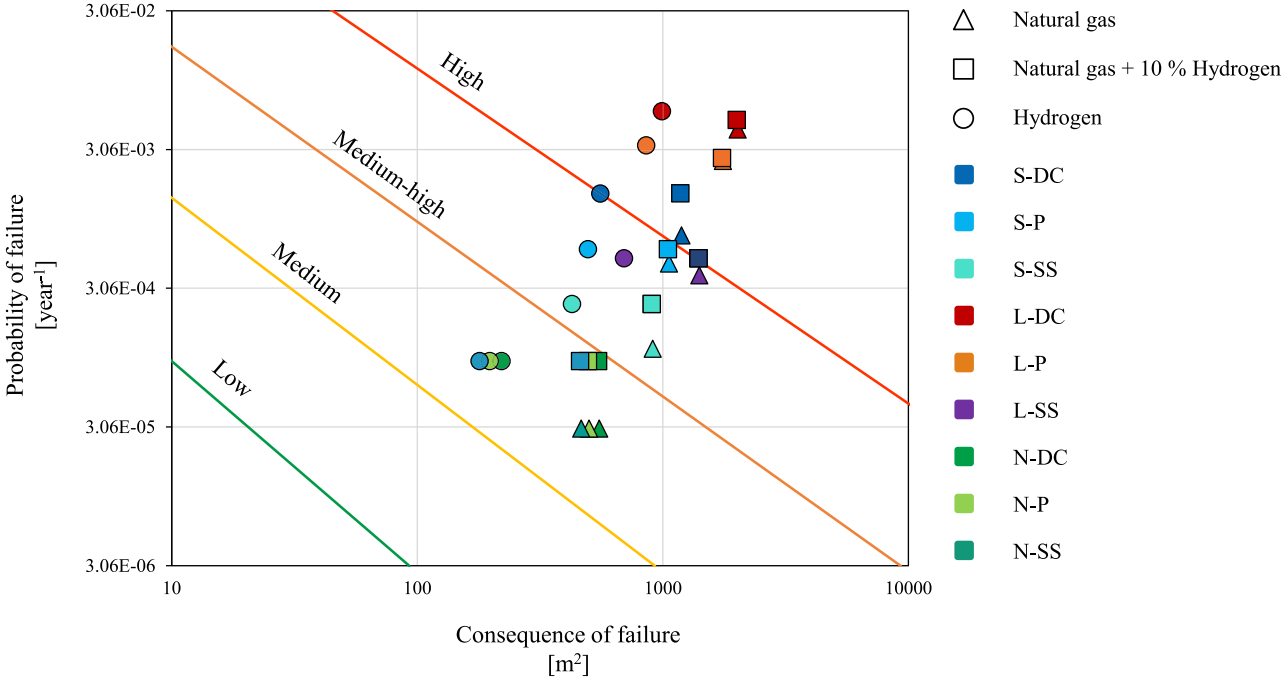

Fig. 8. Iso-risk plot for the pipelines carrying natural gas, hydrogen, or natural gas with 10 $\%_{vol}$ hydrogen.

eventually followed by UT or RT, can be postponed. Moreover, the D_f^{fat} is acceptable in the case of natural gas transport and results in low failure probabilities for each pipeline leg. However, the P_f tends to increase in hydrogen environments, posing a potential risk. Notably, pipeline N is seamless extruded instead of longitudinally welded. This different manufacturing technique should increase fatigue performance by minimizing the presence of welds possibly susceptible to hydrogen-induced degradation. Table 8 indicates the inspection plan to monitor the external thinning of the pipelines, specifying the task, its effectiveness, and the recommended date.

In general, reducing the pipelines' operating pressure can mitigate the safety concerns associated with the reduced lifetime of the infrastructure due to corrosion and mechanical fatigue (Han et al., 2023). However, this modification is not without its challenges. On a volume basis, hydrogen's energy density is 3.3 times lower than natural gas at standard conditions, and lowering the H_2 pressure can only exacerbate this difference (NIST, 2024). This means that the existing pipeline network, repurposed for hydrogen transport, will not be sufficient to deliver the energy required by the end users. The financial and environmental implications are significant, requiring the construction of new pipelines and alternative transport modes.

6. Conclusion

An ad-hoc methodology for risk-based inspection planning of hydrogen technologies is developed. The standardized RBI is complemented by a machine-learning model capable of predicting the influence of pressurized hydrogen gas on mechanical fatigue. The ML model uses the characteristics of the structural material and the component's operating conditions to predict the Fatigue Acceleration Factor and assign a severity class to the equipment. This factor increases the probability of failure of the components exposed to hydrogen gas, thus modifying the risk-based ranking. The GBM classifier is 94.61 % accurate in predicting whether the severity is negligible, low, medium, high, or extreme. In addition, it achieves satisfactory Precision and Recall, particularly for the first three classes. High and extreme severities are predicted with lower Precision and Recall due to the unbalanced training dataset and the complexity of crack propagation under the unstable regime. The feature ranking shows how the amplitude of pressure fluctuations and the nominal pressure of the pipeline are critical parameters for hydrogen-induced fatigue acceleration. In contrast, the ultimate tensile strength and chemical composition slightly influence the fatigue life in H_2 environments. Furthermore, the correlation analysis highlights the relationships between different features and features and labels and shows how the steel grade is the most meaningful material parameter.

Three pipelines with different operating conditions and materials are considered to validate the proposed methodology. The RBI assessment is conducted for each pipeline leg, assuming to transport natural gas, hydrogen, or a blend of natural gas and hydrogen. The results show that external corrosion can be limited through non-intrusive inspections, while periodic monitoring activities cannot reduce mechanical fatigue. The pipelines' operating conditions are appropriate for natural gas transport but are excessively severe in H_2 environments due to the hydrogen-enhanced fatigue crack growth. Line packing pressure fluctuations are responsible for load cycles that can reduce the expected lifetime of the components. The damage factor for mechanical fatigue can increase 50-fold in the pipeline legs downstream of the compression station. For this reason, the working conditions of H_2 transport pipelines should be appropriately reassessed. However, different operating conditions can reduce the pipelines' degradation but also have financial, environmental, and technical implications that should be considered.

In conclusion, the HyRIS methodology can facilitate the risk-based inspection planning of hydrogen technologies, overcoming the limitations of the existing RBI standards. Data-driven predictions can reduce arbitrary evaluations by safety experts regarding the failure probability of hydrogen handling equipment. In addition, this approach is versatile and can be used for various industrial components. The hydrogen-metal compatibility database can be dynamically updated with additional test results, enhancing the model's prediction capability. Nevertheless, the influence of hydrogen environments on mechanical fatigue should be appropriately considered in the next edition of the RBI standards.

Table 8
Inspection plan for external thinning.

ID	Inspection task	I_E	Inspection date
S-DC	95VT + UT/RT	High	17.08.2025
S-P	30VT + UT/RT	Fair	03.12.2032
S-SS	30VT + UT/RT	Fair	26.02.2045
L-DC	95VT + UT/RT	High	01.01.2024
L-P	95VT + UT/RT	High	01.01.2024
L-SS	30VT + UT/RT	Fair	22.10.2041
N-DC	30VT + UT/RT	Fair	18.04.2050
N-P	30VT + UT/RT	Fair	18.04.2050
N-SS	30VT + UT/RT	Fair	18.04.2050

CRediT authorship contribution statement

Alessandro Campari: Writing – review & editing, Writing – original draft, Visualization, Software, Methodology, Investigation, Formal analysis, Data curation, Conceptualization. **Chiara Vianello:** Writing – review & editing, Software, Investigation, Formal analysis, Data curation. **Federico Ustolin:** Writing – review & editing, Supervision. **Antonio Alvaro:** Writing – review & editing, Supervision, Project administration, Investigation. **Nicola Paltrinieri:** Writing – review & editing, Supervision, Resources, Project administration, Funding acquisition.

Declaration of Competing Interest

The authors declare that they have no known competing financial interests or personal relationships that could have appeared to influence the work reported in this paper.

Acknowledgments

This work was undertaken as a part of the research project SH_2IFT-2 (Safe Hydrogen Fuel Handling and Use for Efficient Implementation 2), and the authors would like to acknowledge the financial support of the Research Council of Norway (Grant No. 327009).

References

Abbassi, R., Arzaghi, E., Yazdi, M., Aryai, V., Garaniya, V., Rahnamayiezekavat, P., 2022. Risk-based and predictive maintenance planning of engineering infrastructure: existing quantitative techniques and future directions. Process Saf. Environ. Prot. 165, 776–790. https://doi.org/10.1016/j.psep.2022.07.046.

Abubakirov, R., Yang, M., Khakzad, N., 2020. A risk-based approach to determination of optimal inspection intervals for buried oil pipelines. Process Saf. Environ. Prot. 134, 95–107. https://doi.org/10.1016/j.psep.2019.11.031.

Alvaro, A., Brocks Hagen, A., Lervåg, M., Nyhus, B., Olden, V., 2021. Materials testing and characterization of four X60-X65 pipeline steels.

Alvaro, A., Wan, D., Olden, V., Barnoush, A., 2019. Hydrogen enhanced fatigue crack growth rates in a ferritic Fe-3 wt%Si alloy and a X70 pipeline steel. Eng. Fract. Mech. 219, 106641 https://doi.org/10.1016/j.engfracmech.2019.106641.

American Petroleum Institute, 2016a. API RP 580 - Risk-Based Inspection.

American Petroleum Institute, 2016b. API 579-1/ASME FFS-1 - Fitness-For-Service.

American Petroleum Institute, 2018. API Specification 5L - Line Pipe.

American Petroleum Institute, 2019. API RP 581 - Risk-Based Inspection Methodology.

American Petroleum Institute, 2020. API RP 571 - Damage Mechanisms Affecting Fixed Equipment in the Refining Industry.

American Petroleum Institute, 2024. API RP 574 - Inspection Practices for Piping System Components.

ASME International, 2019. ASME B31.12 - Hydrogen Piping and Pipelines.

ASTM International, 2023. E 647 - Standard Test Method for Measurement of Fatigue Crack Growth Rates.

Baker, W.E., Cox, P.A., Kulesz, J.J., Strehlow, R.A., Westine, P.S., 1983. Explosion Hazards and Evaluation, First ed. Elsevier, New York, New York, United States.
Barnoush, A., Vehoff, H., 2010. Recent developments in the study of hydrogen embrittlement: hydrogen effect on dislocation nucleation. Acta Mater. 58, 5274–5285. https://doi.org/10.1016/j.actamat.2010.05.057.
Brink, H., Richards, J.W., Fetherolf, M., 2016. Real-World Machine Learning, First ed. Manning Publications, Shelter Island, New York, United States.
Campari, A., Alvaro, A., Ustolin, F., Paltrinieri, N., 2023a. Toward Risk-based Inspection of Hydrogen Technologies: a Methodology for the Calculation of the Damage Factor for Hydrogen Embrittlement. Chem. Eng. Trans. 98, 165–170. https://doi.org/10.3303/CET2398028.
Campari, A., Alvaro, A., Ustolin, F., Paltrinieri, N., 2023. Calculation of the damage factor for the hydrogen-enhanced fatigue in the RBI framework. Proc. 33rd Eur. Saf. Reliab. Conf. 437–444. https://doi.org/10.3850/978-981-18-8071-1_p022-cd.
Campari, A., Darabi, M., Alvaro, A., Ustolin, F., Paltrinieri, N., 2023c. A Machine Learning Approach to Predict the Materials ' Susceptibility to Hydrogen Embrittlement. Chem. Eng. Trans. 99, 193–198. https://doi.org/10.3303/CET2399033.
Campari, A., Nakhal Akel, A.J., Ustolin, F., Alvaro, A., Ledda, A., Agnello, P., Moretto, P., Patriarca, R., Paltrinieri, N., 2023. Lessons learned from HIAD 2.0: inspection and maintenance to avoid hydrogen-induced material failures. Comput. Chem. Eng. 173, 108199 https://doi.org/10.1016/j.compchemeng.2023.108199.
Campari, A., Ustolin, F., Alvaro, A., Paltrinieri, N., 2023. A review on hydrogen embrittlement and risk- based inspection of hydrogen technologies. Int. J. Hydrog. Energy 48 (90), 35316–35346. https://doi.org/10.1016/j.ijhydene.2023.05.293.
CCPS, 2010. Guidelines for Vapor Cloud Explosions, Pressure Vessel Burst, BLEVE and Flash Fires Hazards. Wiley, Clifton, New Jersey, United States.
Chatzimarkakis, J., Levoyannis, C., van Wijk, A., Wouters, F., 2021. Hydrogen Act - Towards the Creation of the European Hydrogen Economy.
Chinchor, N., 1992. Evaluation Metrics. Proc. 4th Conf. Messag. Underst. (MUC 4) 22–29. https://doi.org/10.3115/1072064.1072067.
Defteraios, N., Kyranoudis, C., Nivolianitou, Z., Aneziris, O., 2020. Hydrogen explosion incident mitigation in steam reforming units through enhanced inspection and forecasting corrosion tools implementation. J. Loss Prev. Process Ind. 63 https://doi.org/10.1016/j.jlp.2019.104016.
Drexler, E.S., Slifka, A.J., Amaro, R.L., Sowards, J.W., Connolly, M.J., Martin, M.L., Lauria, D.S., 2019. Fatigue testing of pipeline welds and heat-affected zones in pressurized hydrogen gas. J. Res. Natl. Inst. Stand. Technol. 124, 1–19. https://doi.org/10.6028/jres.124.008.
European Gas Pipeline Incident Data Group, 2018. 10th Report of the European Gas Pipeline Incident Data Group (1970 – 2016).
Fetters, K.L., 1964. The Nature of Fatigue. J. Pet. Technol. 16, 869–872.
Friedman, J.H., 2001. Greedy function approximation: a gradient boosting machine. Ann. Stat. 29, 1189–1232. https://doi.org/10.1214/aos/1013203451.
Gangloff, R.P., Wei, R.P., 1974. Gaseous hydrogen assisted crack growth in 18 nickel maraging steels. Acta Mater. 1, 661–667.
Giannini, L., Jafarzadeh, S., Campari, A., Ustolin, F., Paltrinieri, N., 2023. Inspection planning in the marine sector, a case study of a hydrogen-fueled fishing vessel. Proc. Int. Conf. Offshore Mech. Arct. Eng. - OMAE 2023 1–9. https://doi.org/10.1115/OMAE2023-100914.
Glassman, I., Yetter, R.A., Glumac, N.G., 2014. Combustion, Fifth ed. Academic Press, Whatam, Massachusetts, United States.
Goodfellow, I., Bengio, Y., Courville, A., 2016. Deep Learning. MIT Press, Cambridge, Massachusetts, United States.
Han, Z., Li, X., Chen, G., 2023. A stochastic model for RUL prediction of subsea pipeline subject to corrosion-fatigue degradation. Process Saf. Environ. Prot. 178, 739–747. https://doi.org/10.1016/j.psep.2023.08.042.
Holbrook, J.H., Cialone, H.J., Mayfield, M.E., Scott, P.M., 1982. Effect of hydrogen on low-cycle-fatigue life and subcritical crack growth in pipeline steels. Natl. Tech. Rep. Libr. 141.
Howell, K.B., 2017. Principles of Fourier Analysis, Second ed. CRC Press, New York, New York, United States.
Huang, Y., Qin, G., Yang, M., 2023. A risk-based approach to inspection planning for pipelines considering the coupling effect of corrosion and dents. Process Saf. Environ. Prot. 180, 588–600. https://doi.org/10.1016/j.psep.2023.10.025.
International Energy Agency, 2023. World Energy Outlook 2023.
James, G., Witten, D., Hastie, T., Tibshirani, R., Taylor, J., 2023. An Introduction to Statistical Learning with Applications in Python, Second ed. Springer, New York, New York, United States.
Kaplan, S., Garrick, B.J., 1981. On the quantitative definition of risk. Risk Anal. 1, 11–27. https://doi.org/10.1111/j.1539-6924.1981.tb01350.x.
Kim, S., Shin, S., Hwang, B., 2022. Machine learning approach for prediction of hydrogen environment embrittlement in austenitic steels. J. Mater. Res. Technol. 19, 2794–2798. https://doi.org/10.1016/j.jmrt.2022.06.046.
Komoda, R., Yamada, K., Kubota, M., Ginet, P., Barbier, F., Furtado, J., Prost, L., 2019. The inhibitory effect of carbon monoxide contained in hydrogen gas environment on hydrogen-accelerated fatigue crack growth and its loading frequency dependency. Int. J. Hydrog. Energy 44, 29007–29016. https://doi.org/10.1016/j.ijhydene.2019.09.146.
LaChance, J., Tchouvelev, A., Engebo, A., 2011. Development of uniform harm criteria for use in quantitative risk analysis of the hydrogen infrastructure. Int. J. Hydrog. Energy 36, 2381–2388. https://doi.org/10.1016/j.ijhydene.2010.03.139.
Lancaster, J.F., 1999. Metallurgy of Welding, Sixth ed. Woodhead Publishing Ltd, Cambridge, United Kingdom.
Laureys, A., Depraetere, R., Cauwels, M., Depover, T., Hertelé, S., Verbeken, K., 2022. Use of existing steel pipeline infrastructure for gaseous hydrogen storage and transport: a review of factors affecting hydrogen induced degradation. J. Nat. Gas. Sci. Eng. 101 https://doi.org/10.1016/j.jngse.2022.104534.
Lee, F.P., 2001. Loss Prevention in the Process Industries: Hazard Identification, Assessment and Control. Butterworth-Heinemann, Oxford, United Kingdom.
Li, X., Liu, Y., Han, Z., Chen, G., 2024. A risk-based maintenance decision model for subsea pipeline considering pitting corrosion growth. Process Saf. Environ. Prot. 184, 1306–1317. https://doi.org/10.1016/j.psep.2024.02.072.
Lipiäinen, S., Lipiäinen, K., Ahola, A., Vakkilainen, E., 2023. Use of existing gas infrastructure in European hydrogen economy. Int. J. Hydrog. Energy 48, 31317–31329. https://doi.org/10.1016/j.ijhydene.2023.04.283.
Mason, L., Baxter, J., Bartlett, P., Frean, M., 1999. Boosting algorithms as gradient descent. Adv. Neural Inf. Process. Syst. 12 (NIPS 1999), 512–518. https://doi.org/10.1103/PhysRevD.91.072004.
Murphy, K.P., 2012. Machine Learning: A Probabilistic Perspective, First ed. MIT Press, Cambridge, Massachusetts, United States.
Nanninga, N., Slifka, A., Levy, Y., White, C., 2010. A review of fatigue crack growth for pipeline steels exposed to hydrogen. J. Res. Natl. Inst. Stand. Technol. 115, 437–452. https://doi.org/10.6028/jres.115.030.
Nelson, H.G., 1976. On the mechanism of hydrogen-enhanced fatigue crack growth in ferritic steels. Proc. Second Int. Conf. Mech. Behav. Mater.
NIST, 2024. NIST Chemistry WebBook [WWW Document]. NIST Stand. Ref. Database Number 69. URL ⟨https://webbook.nist.gov/chemistry/⟩ (accessed 01.01.24).
Norwegian Ministry of Petroleum and Energy, 2020. The Norwegian Government's hydrogen strategy.
Park, G.T., Koh, S.U., Jung, H.G., Kim, K.Y., 2008. Effect of microstructure on the hydrogen trapping efficiency and hydrogen induced cracking of linepipe steel. Corros. Sci. 50, 1865–1871. https://doi.org/10.1016/j.corsci.2008.03.007.
Phan, H.C., Le-Thanh, L., Nguyen-Xuan, H., 2021. A semi-empirical approach and uncertainty analysis to pipes under hydrogen embrittlement degradation. Int. J. Hydrog. Energy 47, 5677–5691. https://doi.org/10.1016/j.ijhydene.2021.11.166.
Pipeline and Hazardous Materials Safety Administration, 2022. Pipeline Incident 20 Year Trends https://www.phmsa.dot.gov/data-and-statistics/pipeline/pipeline-incident-20-year-trends(accessed 01.01.2024).
Rachman, A., Ratnayake, R.M.C., 2019. Machine learning approach for risk-based inspection screening assessment. Reliab. Eng. Syst. Saf. 185, 518–532. https://doi.org/10.1016/j.ress.2019.02.008.
San Marchi, C., Somerday, B.P., Nibur, K.A., Stalheim, D.G., Boggess, T., Jansto, S., 2010. Fracture and fatigue of commercial grade api pipeline steels in gaseous hydrogen, in: Proceedings of. ASME 2010 Press. Vessels Pip. Div. 939–948. https://doi.org/10.1115/PVP2010-25825.
Sandia National Laboratories, 2023. Technical Database for Hydrogen Compatibility of Materials. H2 Tools https://h2tools.org/technical-database-hydrogen-compatibility-materials(accessed 01.01.24).
Sasaki, Y., 2007. The truth of the F-measure. Int. Conf. Inf. Retr. 1–6.
Scikit-learn, 2024. GradientBoostingClassifier. URL ⟨https://scikit-learn.org/stable/modules/generated/sklearn.ensemble.GradientBoostingClassifier.html⟩ (accessed 8.1.24).
Shishime, K., Kubota, M., Kondo, Y., 2008. Effect of absorbed hydrogen on the near threshold fatigue crack growth behavior of short crack. Mater. Sci. Forum 567–568 409–412. https://doi.org/10.4028/www.scientific.net/msf.567-568.409.
Slifka, A.J., Drexler, E.S., Amaro, R.L., Lauria, D.S., Hayden, L.E., McCowan, C.N., Sowards, J.W., 2015. Measurements of fatigue crack growth rates of the heat-affected zones of welds of pipeline steels. Proc. ASME 2015 Press. Vessels Pip. Conf. 26–31. https://doi.org/10.1115/pvp2015-45242.
Slifka, A.J., Drexler, E.S., Amaro, R.L., Hayden, L.E., Stalheim, D.G., Lauria, D.S., Hrabe, N.W., 2018. Fatigue measurement of pipeline steels for the application of transporting gaseous hydrogen. J. Press. Vessel Technol. Trans. ASME 140, 1–12. https://doi.org/10.1115/1.4038594.
Somerday, B.P., Sofronis, P., Nibur, K.A., Marchi, C.S., Kirchheim, R., 2013. Elucidating the variables affecting accelerated fatigue crack growth of steels in hydrogen gas with low oxygen concentrations. Acta Mater. 61, 6153–6170. https://doi.org/10.1016/j.actamat.2013.07.001.
Subedi, A., Campari, A., Alvaro, A., Thapa, B.S., Paltrinieri, N., 2023. Evaluation of the factors determining hydrogen embrittlement in pipeline steels: an artificial intelligence approach. Proc. 33rd Eur. Saf. Reliab. Conf. 477–484. https://doi.org/10.3850/978-981-18-8071-1_p510-cd.
Suresh, S., Ritchie, R.O., 1982. Mechanistic dissimilarities between environmentally-influenced fatigue-crack propagation at near-threshold and higher growth rates in lower strength steels. Mater. Sci. 16, 529–538.
Takakuwa, O., Ogawa, Y., Okazaki, S., Matsunaga, H., Matsuoka, S., 2019. Temperature Dependence of Fatigue Crack Growth in Low-carbon Steel under Gaseous Hydrogen. In: Am. Soc. Mech. Eng. Press. Vessel. Pip. Div., pp. 1–6. https://doi.org/10.1115/PVP2019-93451.
Tau, L., Chan, S.L.I., Shin, C.S., 1996. Hydrogen enhanced fatigue crack propagation of bainitic and tempered martensitic steels. Corros. Sci. 38, 2049–2060. https://doi.org/10.1016/S0010-938X(96)89123-2.
Thankachan, T., Prakash, K.S., David, C., 2017. Artificial neural network to predict the degraded mechanical properties of metallic materials due to the presence of hydrogen. Int. J. Hydrog. Energy 42, 28612–28621. https://doi.org/10.1016/j.ijhydene.2017.09.149.
TNO, 2005. Methods for the calculation of physical effects - Yellow book, Third ed. Den Hague, Netherlands.
Toscano, R.G., Raffo, J., Fritz, M., Silva, R.C., Hines, J., Timms, C., 2008. Modeling the UOE pipe manufacturing process. Proc. Int. Conf. Offshore Mech. Arct. Eng. - OMAE 521–528. https://doi.org/10.1115/OMAE2008-57605.

Wang, Y., Cheng, G., Hu, H., Wu, W., 2012. Development of a risk-based maintenance strategy using FMEA for a continuous catalytic reforming plant. J. Loss Prev. Process Ind. 25, 958–965. https://doi.org/10.1016/j.jlp.2012.05.009.

Wang, S., Tang, J., Liu, H., 2017. Feature Selection. in: Encyclopedia of Machine Learning and Data Mining. Springer US, Boston, Massachusetts, United States.

Yamabe, J., Yoshikawa, M., Matsunaga, H., Matsuoka, S., 2016. Effects of hydrogen pressure, test frequency and test temperature on fatigue crack growth properties of low-carbon steel in gaseous hydrogen. Procedia Struct. Integr. 2, 525–532. https://doi.org/10.1016/j.prostr.2016.06.068.

Zhao, J., Chevil, K., Yu, M., Been, J., Keane, S., Van Boven, G., Kania, R., Chen, W., 2016. Statistical analysis on underload-type pipeline spectra. J. Pipeline Syst. Eng. Pract. 7, 1–14. https://doi.org/10.1061/(asce)ps.1949-1204.0000241.

Zou, G., Banisoleiman, K., González, A., Faber, M.H., 2019. Probabilistic investigations into the value of information: a comparison of condition-based and time-based maintenance strategies. Ocean Eng. 188 https://doi.org/10.1016/j.oceaneng.2019.106181.